

Lasers in Manufacturing Conference 2023

Characterization of the bistable melting regime for processing of copper with an NIR laser under LPBF conditions

Marvin Kippels^{a,*}, Daniel Heußen^a, Norbert Pirch^a, Constatin Leon Häfner^{a,b}

Fraunhofer Institute for Laser Technology ILT, Steinbachstraße 15, 52074 Aachen, Germany

^bChair for Laser Technology LLT, Steinbachstraße 15, 52074 Aachen, Germany

Abstract

LPBF of pure copper using an infrared laser is considered challenging because only limited parameter ranges are usable to achieve highest densities (>99.5%). The absorption coefficient of copper for the infrared wavelength is often used as a central influencing parameter but does not reflect the characteristic transition behavior. An abrupt transition to keyhole welding when the energy input is increased limits the usable parameter range. In the present work, the transition behavior is characterized on basis of single weld tracks generated under LPBF conditions. In addition to the process parameters laser power, beam diameter and scanning speed, different surface qualities are included in the consideration of the transition behavior. In this context, a process parameter range defined by a melt pool alternating between heat conduction and keyhole welding is observed. This bistable range can be characterized, among other things, with the quotient of laser power and beam diameter.

Keywords: Keyhole; copper; LPBF; infrared; melt pool stability

1. Introduction

The state of the art for LPBF of pure copper largely comprises empirical investigations to define process parameters in order to produce test specimens with sufficient relative density ($\rho > 99.5\%$). Approaches with increased intensity by a small beam diameter (Stoll et al., 2020) and with increased laser power (Abdelhafiz et al., 2021; Colopi, et al., 2018; Colopi, et al., 2019; Jadhav et al., 2019a; Jadhav et al., 2021) lead to limited process windows. The achieved buildup rates are in the range below 4 mm³/s and the achieved

* Corresponding author. Tel.: +49-241-8906-346.

E-mail address: marvin.kippels@ilt.fraunhofer.de.

relative density in the range of max. 99,5%. Furthermore, all of these works observe deep welding. In particular, Jadhav et al. defines a process window and assigns it to the process area "deep welding" on the basis of an analytical calculated threshold. Experimental data shows that it is not so easy to distinguish between keyhole welding and heat conduction welding and that there are certain instabilities, especially for pure copper welding, and different influencing factors on the behavior, such as the surface condition. This work examines how this transition behaves under different conditions.

Experimental Execution

The following experiments aim to capture the complex transition behavior in copper LPBF between heat conduction welding and keyhole welding. In built LPBF volumes, it is difficult or impossible to obtain knowledge about the welding regime and the weld pool dimensions of the individual weld tracks. Therefore, experiments were carried out with several individual welding tracks on sheet material.

1.1. Conditions

The tests were conducted in a Trumaform LF 130 modified for laboratory use, in which a YLS-1000-SM infrared laser is installed. Fig. 1 (b) shows the second of the two associated process chambers with the opened optical slide above it. The integrated ScanLab varioSCAN 40 allows defocusing during the experiment so that the influence of a larger beam diameter on the melt pool characteristics can be investigated under otherwise identical conditions. The properties of the laser and its beam can be seen in Fig 1 (a) and (c). Argon shielding gas is circulated in the process chamber to reduce the oxygen content below 200 ppm.

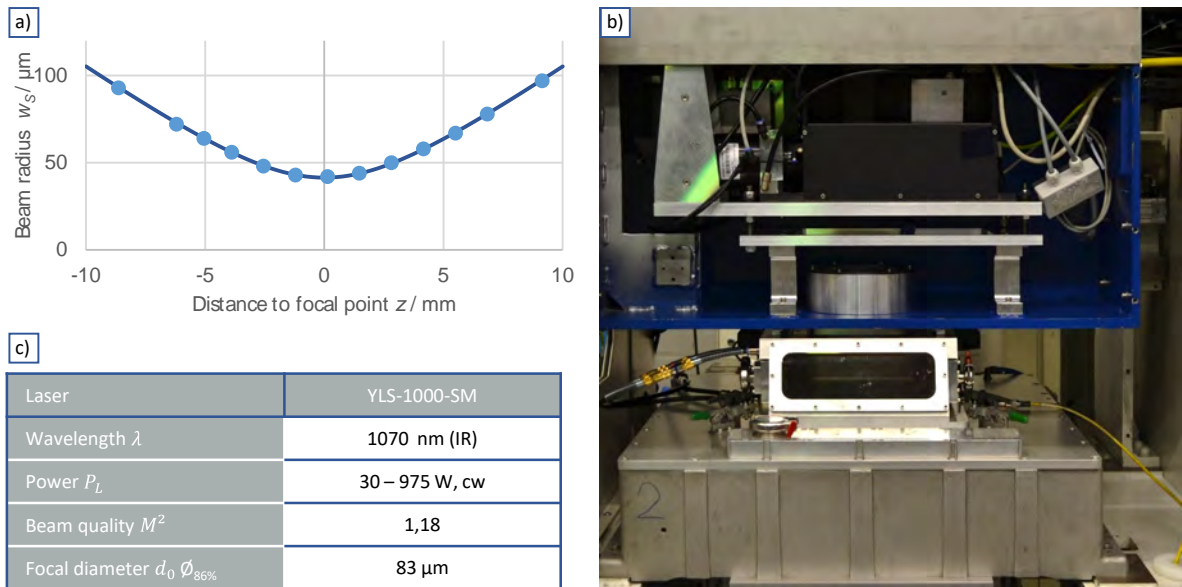


Fig. 1. (a) Beam caustic; (b) process chamber with opened optical slide; (c) characteristics of the infrared laser

Cuts from sheet material (75x75x2mm) made of Cu-ETP (98% IACS) were used as sample material. To reduce distortion of the sample during exposure and, thus, unintentional defocusing of the laser beam on the sample,

the sample was clamped to the underlying substrate plate by a retainer, see Fig. 3 (a). In addition, pauses between 1 to 10 seconds were left between the individual exposures according to the irradiated energy in order to prevent the sample from heating up significantly during the experiment.

In order to determine the impact of surface quality, tests were carried out with sandblasted and polished surfaces and additionally with a powder layer (Cu-OFHC, PSD 16 - 45 μm) on a sandblasted surface, see Fig. 2. Powder was applied by tapping a brush covered in powder above the sample. The homogeneity of the application was checked visually. The layer thickness was approximately 50 μm .

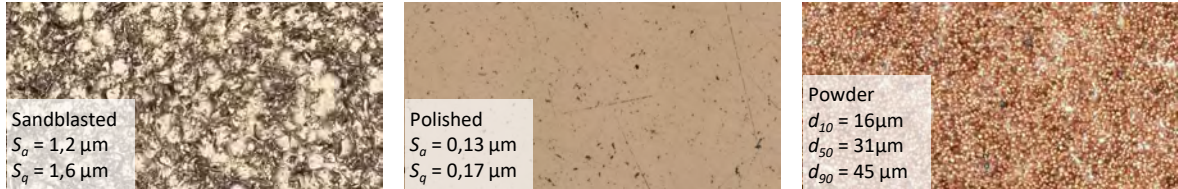


Fig. 2. (a) sandblasted Cu-ETP surface; (b) hand polished Cu-ETP surface; (c) sandblasted Cu-ETP surface with manually applied Cu-OFHC powder

In order to determine the influence of the process parameters on the melt pool behavior the process parameters were varied around a range with bistable melt-pool formation: laser power (from 400 W to 975 W), scanning speed (from 50 mm/s to 1000 mm/s) and beam diameter (from 83 μm to 205 μm). For one parameter combination, 10 vectors with a length of 10 mm and a distance of 0.4 mm from each other were irradiated with the same scanning parameters, see Fig. 3 (b). These multiple melt tracks were used to compensate for the seemingly random variation of the melt pool.

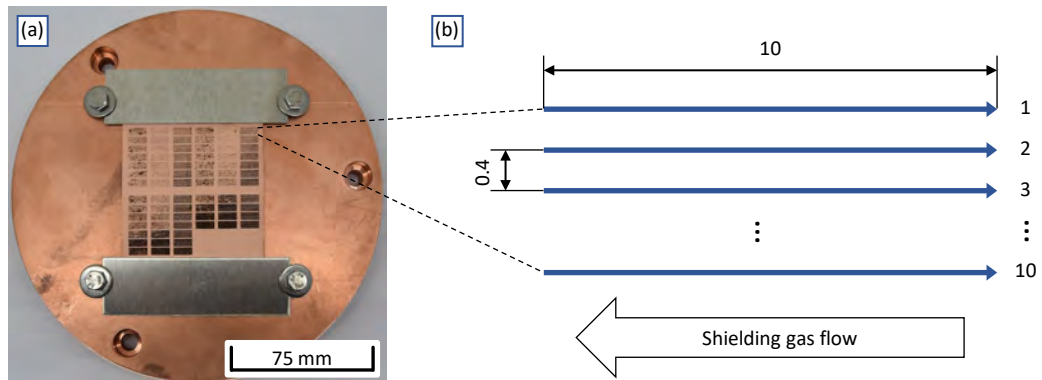


Fig. 3. (a) irradiated sample after depowdering with clamp holder on copper substrate plate; (b) sketch of the irradiation strategy. In the following figures, the scanning direction is always from left to right.

1.2. Data Collection

After irradiation, the top view of the melt tracks was imaged with a 300x magnification using a Keyence VHX-6000 optical microscope. For the quantitative evaluation of the bistable behavior, the percentage of deep welding was measured. For this purpose, the sum of the lengths of the sections with keyhole welding characteristics are divided by the total length of the melt tracks. The differentiation criteria are described in the following chapter. To determine these distinguishing features, metallographic cross-

sections were produced from selected samples. For this purpose, the melt tracks were cut at least 2 mm after the start of the track and hot-mounted in a thermoplastic phenolic resin. The sample was then ground over six stages from P80 to P4000 on a water-cooled metallographic grinding machine. The sample was polished with diamond suspensions of 1 μm and 0.25 μm grit for five minutes at a time. To make the grain structure of the copper visible, the sample was etched for 40 seconds in 1:10 Adler solution. Subsequently, images of the melt track cross-sections were taken under 500x magnification. For evaluation, the melt pool width, depth and cross-sectional area were measured for each track. The dimensions of the melt pool are defined in Fig. 4.

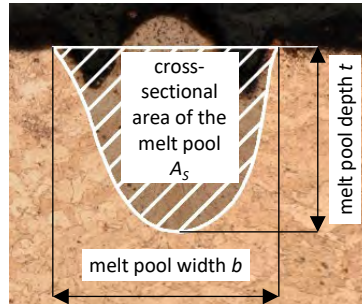


Fig. 4. Definition of the measurands melt pool width, depth and cross-sectional area. The upper edge of the sheet material serves as a reference for both the welding depth and the cross-sectional area. This definition effectively observes the volume that was not previously remelted. This mitigates local variations caused by balling and humping.

2. Analysis of meltpool topology and geometry

A qualitative examination of the melt tracks clearly shows two distinct melting modes. In the lower power range, there is a narrow, smooth melt track without prominent scaling. Fig. 5 shows these heat conduction welding tracks as an exemplary case for a fixed laser power. For higher powers, these characteristics barely change.

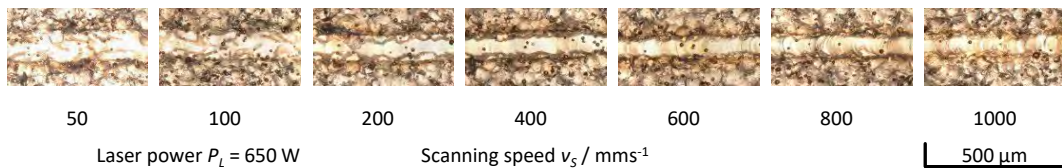


Fig. 5. Heat conduction weld tracks on sandblasted copper without powder at the focal diameter $d_s = 83 \mu\text{m}$ and increasing scanning speed. Visible particles are contributed by the shielding gas flow contaminated with pure copper powder. However, in this small quantity, this can be neglected.

Above a threshold the melt tracks characteristics can change drastically, see Fig 7. Segments of keyhole welding tracks with greater width, pronounced scaling and an overall rougher surface were formed. This distinction is particularly clear at low scanning speeds. Melt pool ejections confirm the presence of a keyhole. At the focal diameter for power levels below 700 W, keyhole welding only starts after a phase of heat conduction welding, so that an effect caused by heating can be assumed here. Higher scanning speeds extend the phase of heat conduction welding and increase this power threshold. Above this threshold, keyhole welding can start immediately with the beginning of the melt track.

The alternation between these modes appears in a stochastic way. Keyhole welding starts abruptly and can end abruptly with a melt pool ejection or gradually return to heat conduction welding over the length of one to two beam diameters, as seen in Fig. 6.

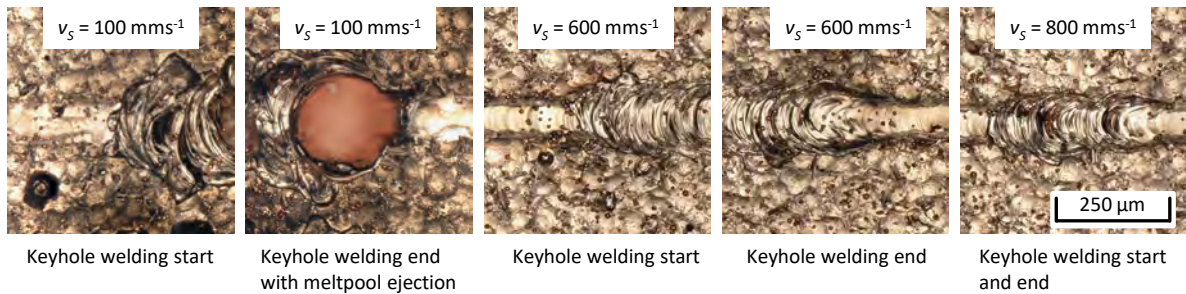


Fig. 6. Starts and ends of keyhole weld tracks without powder application at a laser power of $P_L = 700$ W at the focal diameter $d_s = 83$ μm with increasing scanning speed. The scanning direction is from left to right.

To confirm the distinction based on the appearance of the top view of the melt track, the top view was compared with a cross-sectional view in Fig. 8. The smooth and slim appearing melt tracks show an ellipsoidal cross-section typical for heat conduction welding. In contrast, the scaled, rough and wide melt tracks in the cross-section exhibit a high weld penetration depth with a high aspect ratio, which is characteristic of keyhole welding.

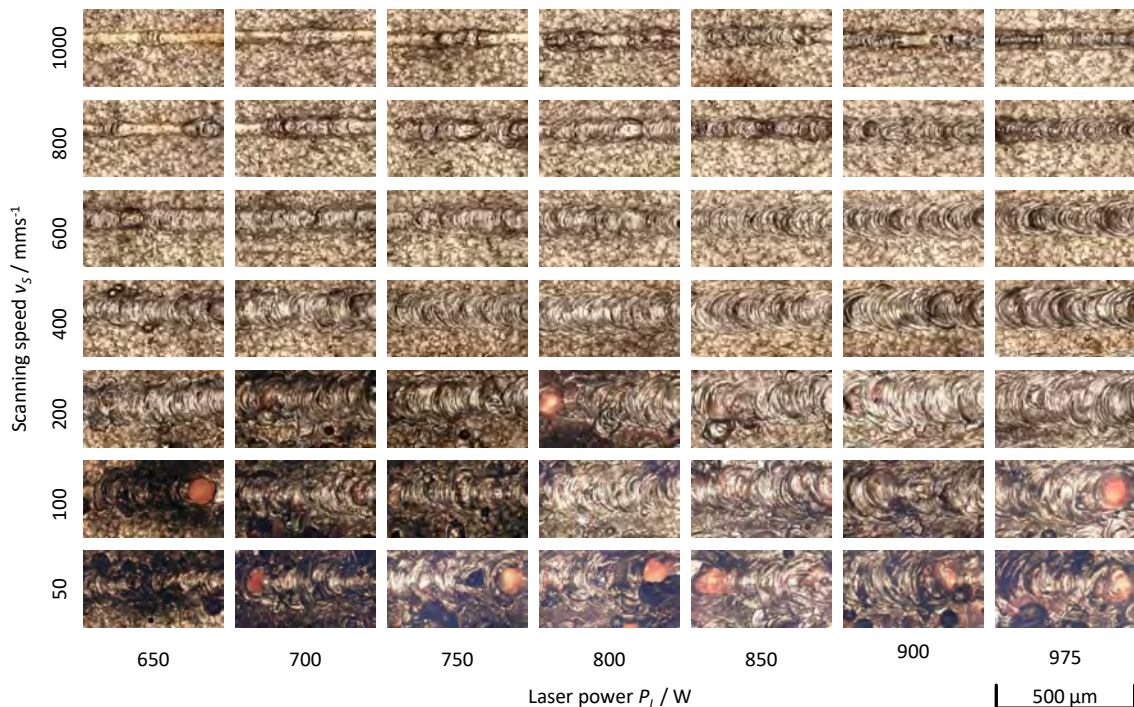


Fig. 7. keyhole weld tracks without powder with increasing scanning speed and power at the focal diameter $d_s = 83$ μm .

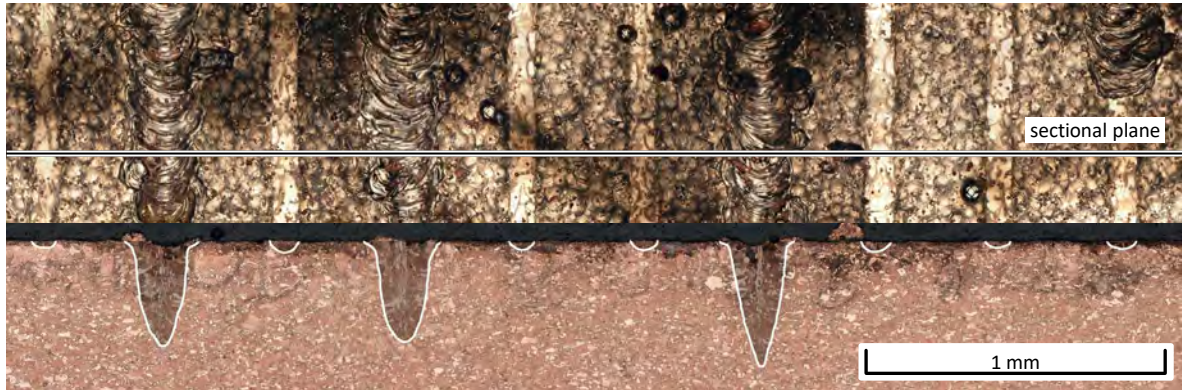


Fig. 8. Composite image a from a top view and a cross-section. The welds in the cross-section are highlighted by a white line.
 $P_L = 650$ W, $v_s = 100$ mm/s, sandblasted Cu-ETP without powder

Diagrams of the generated melt track dimensions can be seen in appendix A. It is noticeable that their sizes scale approximately with the laser power both in deep penetration welding and in heat conduction welding. The influence is greater at lower scan speeds and or in keyhole welding. This has already been described by (Engler, 2015). Furthermore, the influence of the process parameters on the different quantities of melt track geometry appears similar, so that a comparative look at the melt track dimensions seems to be useful. In Fig. 9, the melt pool dimensions of the individual data points are normalized with the beam diameter and plotted against each other. Thereby, correlations between the individual geometry sizes appear in the form of power functions. It is interesting to note that the areas with heat conduction and keyhole welding tracks are separated by a gap. An experimental definition for keyhole welding with an aspect ratio of at least $t/b = 0.5$ could be derived from this.

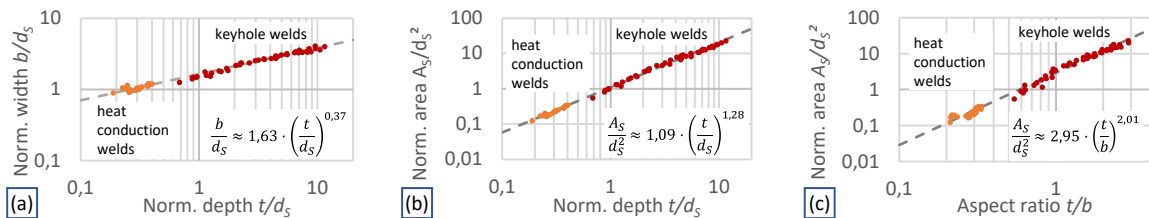


Fig. 9. Comparison of the melt track dimensions with each other normalized by the beam diameter in a double logarithmic reference frame. Each data point refers to a single cross-section. $P_L = 650 - 975$ W, $v_s = 50 - 1000$ mm/s, $d_s = 83$ μ m, sandblasted Cu-ETP without powder; (a) melt track width vs. melt track depth; (b) melt track cross section area vs. melt track depth; (c) melt track cross-sectional area vs. aspect ratio

3. Analysis of keyhole welding percentage

Three process regions can be identified, one consisting of heat conduction welding, one of deep penetration welding and a transition zone of both mixed. The transition region is called bistable because within this region the melting modes alternate stochastically.

The threshold for keyhole welding separates the heat conduction region from the bistable region. This threshold is often given as an intensity in the literature (Seidgazov, 2020; Tenbrock et al., 2020; Matilainen et

al., 2015). However, other publications (Engler, 2015; Rubenchik et al., 2018; Heß, 2012) state the beam parameter quotient

$$Q = \frac{P_L}{d_s} \quad (1)$$

as the decisive factor. Moreover, Engler and Rubenchik et al. derived analytical thermophysical models establishing a proportionality

$$Q_{crit} \sim T_V \cdot \lambda_{th} \quad (2)$$

of the keyhole welding threshold Q_{crit} with the product of the boiling point T_V and the thermal conductivity λ_{th} .

Fig. 10 shows the measured keyhole welding percentage of the tracks produced with variation of laser power and beam diameter versus intensity and beam parameter quotient for a sandblasted surface so that the two quantities can be evaluated.

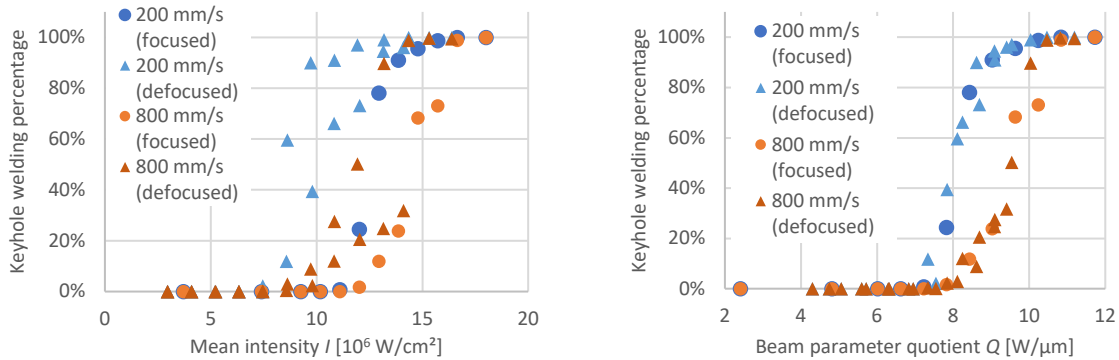


Fig. 10. Comparison of the scaling of the keyhole welding percentage with the mean intensity $I = 4 \cdot P_L / d_s^2$ and the beam parameter quotient $Q = P_L / d_s$. The laser power of the focused beam was varied between 400 W and 975 W. The beam was defocused up to a diameter of 205 μm at two power levels (800 W and 975 W).

This illustration clarifies that the intensity only represents a clear threshold for a fixed beam diameter. When the beam diameter is varied, however, no clear intensity value can be given. The beam parameter quotient clearly determines the threshold and can also indicate the width of the bistable range. At a higher scanning speed, the threshold shifts to a higher value of the beam parameter quotient and the bistable range extends over a larger range. The transition for $v_s = 200$ mm/s ranges from 7.5 to 9 $\text{W}/\mu\text{m}$ and for $v_s = 800$ mm/s from 8 to 10.5 $\text{W}/\mu\text{m}$. At higher scanning speeds, the sections with keyhole welding shorten but are present with higher spatial frequency.

The influence of the surface condition on the keyhole welding percentage is shown in Fig. 11. When the polished and the sandblasted surface are compared, almost no difference in the transition behavior can be observed. Only at higher scanning speeds and a high beam parameter quotient is the amount of keyhole welding for the polished surface marginally lower. However, the behavior changes significantly when powder is applied. The critical threshold for initiating keyhole welding drops to approx. 6 $\text{W}/\mu\text{m}$ nearly independent of the scanning speed, and the transition extends over a smaller range. Nevertheless, the transition is still scaled according to the beam parameter quotient.

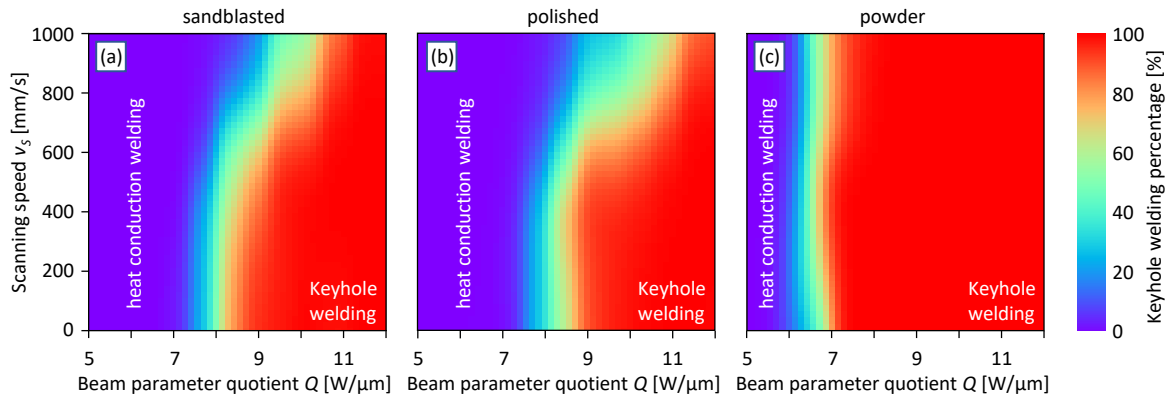


Fig. 11. Influence of the variation of the surface conditions on the keyhole welding percentage. Here a false color representation of the interpolation between measuring points is depicted. The laser power was varied between 400 and 975 W, the scanning speed from 50 to 1000 mm/s and the beam diameter between 83 and 205 μm . (a) Sandblasted surface; (b) polished surface. Here the measurement was conducted only at the focal diameter; (c) sandblasted surface with a 50 μm layer of pure copper powder

4. Comparison with simulation of the critical beam parameter quotient

As an alternative to determining the deep welding threshold by evaluating melting lines, an attempt was made to quantify the threshold via a simulation as a function of the process and material parameters and to compare it with the experimentally determined values. The simulation approach is based on a heat conduction model in which the absorption of the laser power is represented by Neumann boundary conditions. The simulation was carried out for a Gaussian beam, of which 12% is absorbed. This percentage was taken from absorption during heat conduction welding (Behler et al., 2021). The material is modelled with the finite element method by a three-dimensional grid with 8 node hexahedral elements. Due to a gradient-adjusted resolution, the area of the process zone is modelled with significantly finer elements inside than outside. The model considers the temperature dependence of the material parameters: density, thermal conductivity and capacity, and also fusion and vaporization enthalpy (Mills, 2002). A simulation of melt pool dynamics is not incorporated. The transition from heat conduction to deep welding is determined when the boiling temperature is reached in the quasi-steady-state. The simulations are based on in-house software developed at Fraunhofer ILT for process simulations.

Fig. 12 (a) shows the critical parameters when the boiling temperature is reached. It becomes clear that the beam intensity cannot describe this threshold, but the beam parameter quotient can do this well, especially at low scanning speeds. Only at higher scanning speeds can an additional influence of the beam diameter be observed. Therefore, the experimental observations are well supported by the simulation results.

In Fig. 12 (b), the simulated threshold is superimposed on the experimentally measured keyhole welding percentage. There are differences in the absolute value of the beam parameter quotient and in the influence of the scanning speed at higher scanning speeds. These differences can probably be explained by the melt pool dynamics and an error in the assumed absorption value. Furthermore, simply reaching the boiling temperature might not be sufficient to initiate keyhole welding.

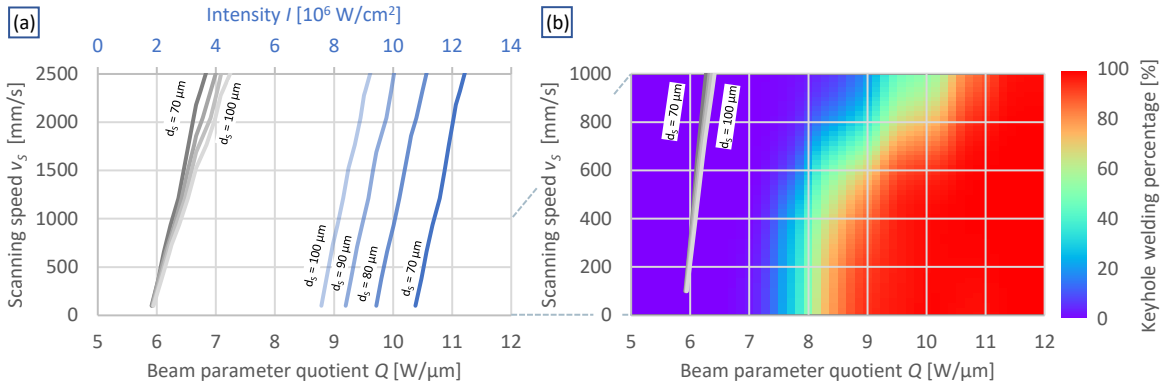


Fig. 12. (a) Simulation results for when the boiling temperature is reached on the surface of bare pure copper bulk material. These parameter combinations can be considered as a critical threshold to initiate deep welding; (b) comparison of simulation results with measured keyhole weld percentage.

5. Discussion

Since pure copper has a low absorption coefficient for infrared laser radiation, high powers used during the LPBF process. Thus, disturbances that increase the degree of coupling can have a high influence on the coupled power. The surface could introduce disturbances due to chemical impurities, e.g. oxides, and roughness. This is particularly noticeable through the interrupted melt track on polished surfaces. On the polished surface (Fig. 16 in appendix B), the coupling was so low that in some cases even heat conduction welding was only initiated by a disturbance. However, no difference above the measurement noise was apparent between the measurements of the keyhole welding percentage with sandblasted and polished surfaces. This shows that the surface quality is not decisive for the initiation of keyhole welding. Thus, the cause is to be found in the preceding heat conduction welding itself. The melt pool is accompanied by a dynamic whose influence can be regarded as a disturbance variable. Assuming that this dynamic produces fluctuations in the coupling, which are stochastically distributed in their magnitude, the bistable behavior can be explained.

To maintain a keyhole, a minimum power must be available below which deep welding is not possible. Above this threshold, keyhole welding is not initiated immediately because the available power does not reach the weld pool due to the low coupling. If the coupling is increased by a sufficiently large disturbance, deep penetration welding can be initiated. If the power is only just above the threshold, a larger disturbance is required to start the process. Since such a disturbance occurs less frequently, the deep welding percentage for such a parameter combination is low. At higher powers, smaller disturbances that occur more frequently are sufficient. At very high power levels, the required power can be coupled in without the need for a disturbance, which results in pure keyhole welding.

A similar argument can be made for the termination of keyhole welding. The keyhole welding process is highly dynamic and can itself cause disturbances that terminate it: either at high energy densities when a vapor bubble forms, which can explosively eject the melt pool if the capillary is constricted, or at lower energy densities when the capillary regresses. In both cases, heat conduction welding follows, as only a new disturbance can initiate the keyhole welding process again.

At high scanning speeds, the melting modes change at a higher spatial frequency. Due to the higher dynamics as a result of the scanning speed, the rate of disturbances is increased and thus the switching is more frequent. The increased dynamics, as seen in Fig. 17 in appendix B, are visible by the tendency to form ridges, undercuts and humping as a result of high scanning speeds. Also, these defects make it difficult to distinguish

between heat conduction and keyhole welding, so only measurements up to scanning speeds of 1000 mm/s were analyzed.

When powder is applied, a clear change in the transition characteristics becomes noticeable. Keyhole welding starts with a lower beam parameter quotient and the transition range is reduced. Likewise, the scanning speed has a reduced influence on the transition. This stabilizing effect of the powder can be explained by an interaction of the powder with the melt pool and the laser radiation, which increases the degree of coupling of the laser radiation more constantly. The higher coupling reduces the influence of disturbances on the initiation of keyhole welding. This is supported by the overall higher power coupling in a powder bed compared to bare metal (Matthews et al, 2018).

6. Conclusion and outlook

The bistable region was experimentally identified in which heat conduction and deep welding occurs in pure copper for the infrared wavelength of $\lambda = 1070$ nm by a determining the keyhole welding percentage of the top view of single melt tracks. In addition, by means of a thermodynamic simulation, the correlation with the keyhole welding threshold could be confirmed with the beam parameter quotient and disproved with the beam intensity. The position of the bistable region scales with the beam parameter quotient. A correlation with the laser beam intensity has been disproved. For higher scanning speeds, the bistable region shifts to higher values of the beam parameter quotient and widens. In addition, the surface influence was investigated on the bistability by repeating the tests with a copper sample with polished surface and with powder application. The results without powder application show only marginally quantitative differences of the deep welding percentage. From this it was concluded that the bistability stems from the dynamics of the melt pool. The transition behavior from heat conduction to deep welding was explained with a perturbation model.

When powder was applied, both the critical beam parameter quotient as well as the range of bistability are reduced and the scanning speed has a lower influence on the keyhole welding percentage. Thus, powder has a stabilizing influence on the welding process, caused by a constantly higher power coupling. The direct transferability to the LPBF process is limited by the simplifications made (single tracks, manual powder application, exposure pauses, the exposure of a single layer on sheet metal). Nevertheless, the underlying mechanisms of the bistable range and the scaling with the beam parameter quotient can be transferred.

A clear correlation of the melt pool sizes (width, depth, area, aspect ratio) can be seen. The relationships between these quantities can be described by power laws and apply to both melting modes. The relationship of the melt pool dimensions across the two melting modes is remarkable, as distinctly different melt pool dynamics of the are present in both. However, the transition between the two modes is characterized by a gap, where no melt pools could be measured. This gap indicates that for a process with pure copper and infrared laser radiation, there is no stable transition mode between heat conduction and keyhole welding. This power laws could be used in order to determine melt pool depth and cross-sectional area only by the melt pool width measured by a top view. Furthermore, a process efficiency defined by the melting enthalpy of the cross-sectional area and the irradiated laser power could be calculated alone with the measured melt pool width.

References

- Abdelhafiz, M., et al., 2021. Process-Structure-Property Relationships of Copper Parts Manufactured by Laser Powder Bed Fusion, in *"Materials"*, 14, 2945.
- Behler, K. et al., 2021. Energy coupling in laser powder bed fusion of copper using different laser wave-lengths, in: *"Lasers in Manufacturing"*.

- Colopi, M. et al., 2018. Selective laser melting of pure Cu with a 1 kW single mode fiber laser, in "Procedia CIRP", 74, p. 59–63.
- Colopi, M. et al., 2019. Limits and solutions in processing pure Cu via selective laser melting using a high-power single-mode fiber laser, in "The International Journal of Advanced Manufacturing Technology", 104, p. 2473–2486.
- Engler, S. M., 2015. Laserstrahlschweißen von Kupferwerkstoffen mit brillanten Strahlquellen im infraroten und grünen Wellenlängenbereich, dissertation, RWTH Aachen.
- Heß, A., 2012. Vorteile und Herausforderungen beim Laserstrahlschweißen mit Strahlquellen höchster Fokussierbarkeit, dissertation, Universität Stuttgart.
- Jadhav, S. D. et al., 2019a. Influence of selective laser melting process parameters on texture evolution in pure copper, in "Journal of Materials Processing Technology", 270, p. 47–58.
- Jadhav, S. D., et al., 2021. Laser-based powder bed fusion additive manufacturing of pure copper, in "Additive Manufacturing", 42, 101990.
- Matilainen, V. et al., 2015. Preliminary Investigation of Keyhole Phenomena during Single Layer Fabrication in Laser Additive Manufacturing of Stainless Steel, in: "Physics Procedia", 78, p. 377-387.
- Matthews, M. et al., 2018. Direct measurements of laser absorptivity during metal melt pool formation associated with powder bed fusion additive manufacturing processes, in: "Journal of Laser Applications", 30, 032302.
- Mills, K., 2002. Recommended values of thermophysical Properties for selected com-mercial alloys, Woodhead Publishing Limited, ISBN: 978-1-85573-569-9.
- Rubenchik, A. M. et al., 2018. Scaling laws for the additive manufacturing, in: "Journal of Materials Processing Technology", 257, p. 234-243.
- Seidgazov, R. D., Mirzade, F. K., 2020. Threshold conditions for thermocapillary transition to deep penetration mode in selective laser melting of metal powder bed, in: "IOP Conference Series: Materials Science and Engineering", 759, 012023.
- Stoll, T. et al., 2020. Process development for laser powder bed fusion of pure copper, in: "Laser 3D Manufacturing VII", 11271, p. 46.
- Tenbrock, C. et al., 2020. Influence of keyhole and conduction mode melting for top-hat shaped beam profiles in laser powder bed fusion in: "Journal of Materials Processing Technology", 278, 116514.

Appendix A. Melt pool dimensions

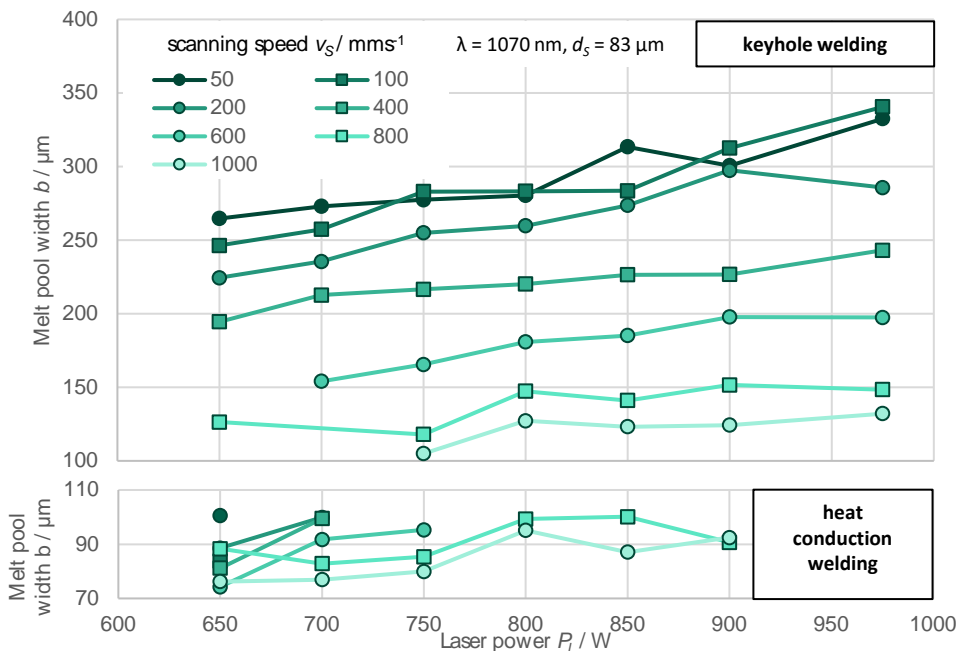


Fig. 13. Melt pool depth of keyhole and heat conduction welds at focal beam diameter on sandblasted copper-ETP.

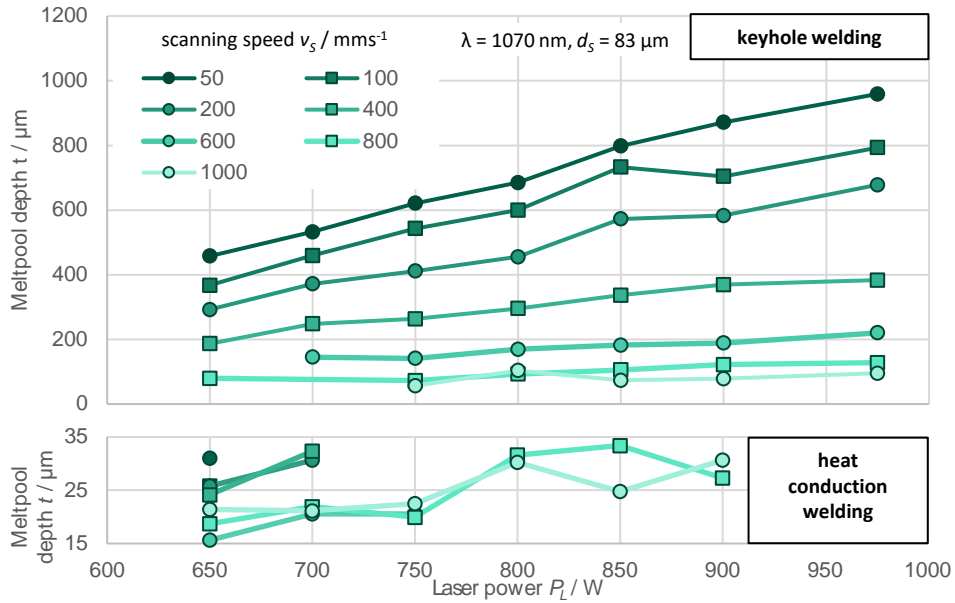


Fig. 14. Melt pool depth of keyhole and heat conduction welds at focal beam diameter on sandblasted copper-ETP.

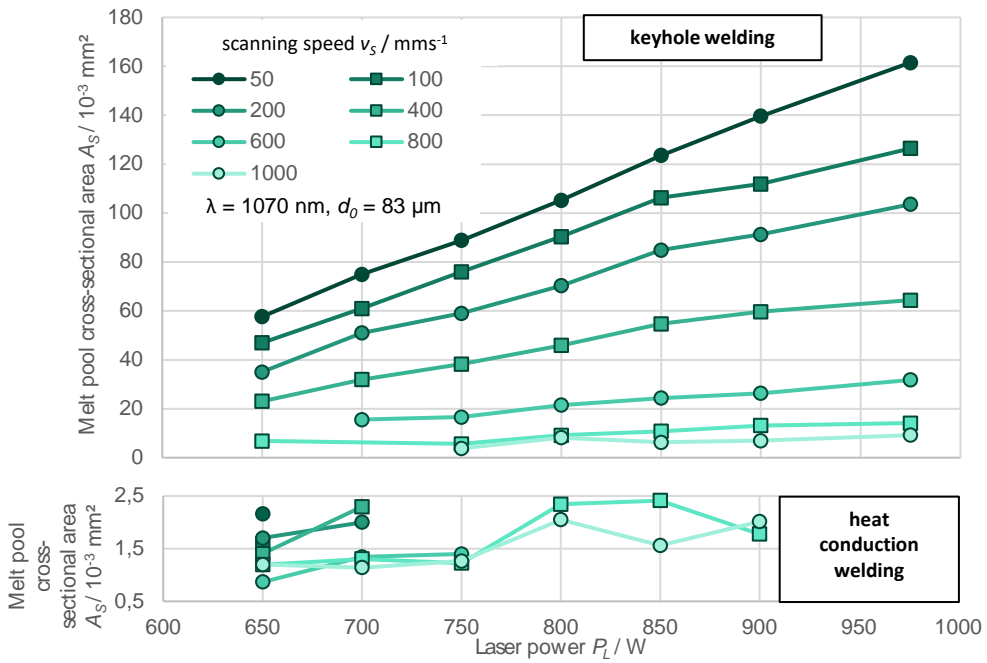


Fig. 15. Melt pool cross-sectional area of keyhole and heat conduction welds at focal beam diameter on sandblasted copper-ETP.

Appendix B. Melt pool dimensions



Fig. 16. Interrupted melt tracks due to the high reflectance of the polished copper ETP. Heat conduction and keyhole welding triggered by a large visible scratch. $P_L = 650$ W, $v_s = 400$ mm/s, $d_s = 83$ μ m.

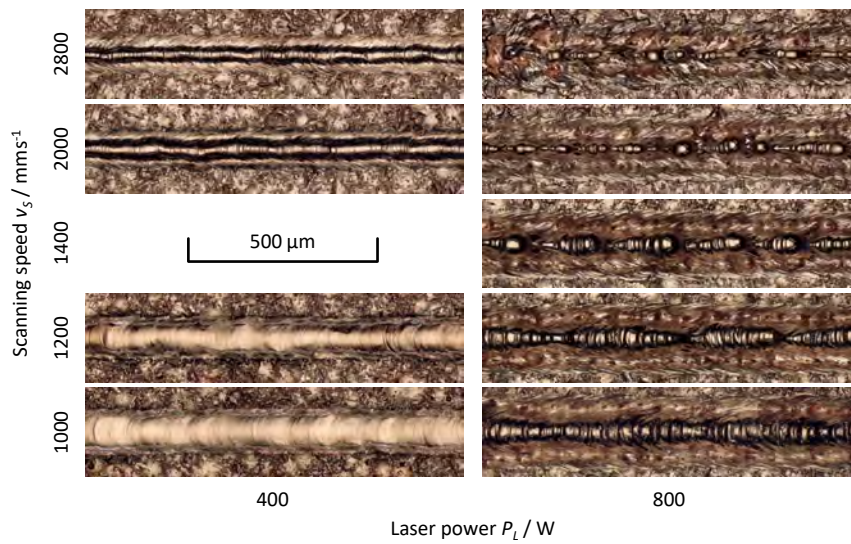


Fig. 17. Increased melt pool dynamics due to higher scanning speeds at focal beam diameter $d_s = 83$ μ m on sandblasted copper-ETP.